Solid Freeform Fabrication 2024: Proceedings of the 35th Annual International Solid Freeform Fabrication Symposium – An Additive Manufacturing Conference
Reviewed Paper

Influence of Scanning Strategy on the Microstructure and the Mechanical Properties of AlSi10Mg Parts Fabricated via LPBF

S. J. Dietrich*, A. V. Hamm*, L. Englert*

* Institute for Applied Materials – Materials Science and Engineering, Karlsruhe Institute of Technology, Karlsruhe 76131, Germany

Abstract

Laser powder bed fusion (LPBF) of AlSi10Mg is a widely used combination in the area of Additive Manufacturing (AM). Nonetheless, the influence of different scanning strategies on the properties of AlSi10Mg parts has not been considered extensively. In this study, a total of 15 different scanning strategies has been investigated, including various non-standard scan patterns, contour sequences, re-melting strategies, and layer rotation angles. The results reveal a significant difference between scan strategies regarding porosity, pore morphology and surface roughness. Tensile tests were used to map the microstructural and surface topography differences of the samples to the mechanical material behavior. The findings show that the measured density does not correlate with the expected tensile strength, the critical factor rather appears to be the pore morphology. Overall, the findings contribute to understanding the influence and usability of scanning strategies in LPBF manufacturing to reach optimized material properties in AM parts.

Introduction

Laser powder bed fusion (LPBF or also PBF-LB) of metal powders requires a high laser power to create a melt pool, which is a particular challenge when using aluminum due to the high reflectivity and thermal conductivity of the material. Due to interactions within the melt pool and the laser exposure strategy, defects are a common result in LPBF microstructures and parts. The defects created during the LPBF process can be roughly divided into two types: metallurgical pores and irregular pores. The metallurgical pores are often small (<100 µm) and have a spherical shape, while the irregular pores can also be larger (>100 µm) and have anisotropic morphologies (Aboulkhair et al., 2014). Due to their spherical shape and relatively smooth surface, the formation of metallurgical pores (also known as "hydrogen porosity") is most likely either due to moisture or due to inclusions of inert gas in the melt pool or to pre-existing gas inclusions within the powder particles that are released during melting. These metallurgic pores form the majority of the pores found globally in the components. Irregular pores, on the other hand, can vary greatly in size and shape. They are caused by various mechanisms: by unmolten or insufficiently melted powder that does not bond, (such pores are therefore also referred to as lack-of-fusion pores) or by melt pool instabilities (Aboulkhair et al., 2014; Leonard et al., 2016). Spherical pores can be also be caused by the keyhole effect, which leads to the so-called keyhole pores. The keyhole pores, can be explained by the depression (also known as a vapor capillary) created on the surface of the melt pool due to the metal evaporation and the resulting recoil pressure. The depth of this vapor capillary depends on the laser power and scanning speed and reaches its maximum when the scanning speed approaches zero. After the energy introduced by the laser beam is removed, the melt pool depression collapses and traps gas in spherical pores, as the system cannot stabilize again so quickly (Martin et al., 2019).

In the case of aluminum alloys, insufficient melting of powder and thus the creation of lack-of-fusion pores can also be due to oxide layer formation. These are caused by the high reactivity of aluminum with oxygen on the surface of the particles or during the process on the surface of the melt pool and can prevent repeated melting of the powder, as the laser power can be insufficient to melt the oxide layer or the wetting of molten powder on oxide layers is insufficient. As a result, spaces are formed with enclosed powder or oxides that have an irregular shape. This effect occurs more frequently with recycled powder than with fresh powder, but can be observed with both powder characteristics (Tradowsky et al., 2016). Lack-of-fusion pores can also be caused by problems with the production system or unsuitable laser scanning strategies, for example insufficient distribution of the metal powder on the build platform or an inconsistent hatch spacing/laser power relation. This often leads to balling of the melt track, which can be avoided by maintaining a low oxygen content in the chamber during the manufacturing process and by adjusting the scanning speed to the laser power (Aboulkhair et al., 2016). In Al alloys, irregular pores also often form at the ends of the scan paths or at the turning points where the laser is decelerating at constant power and therewith creating a turbulent melt bath as discussed via the keyhole effect.

Different laser exposure strategies/scan patterns, according to the described mechanisms of defect formation above, have a powerful effect on porosity formation. The most frequently used scan patterns are shown in Figure 1a) - f).

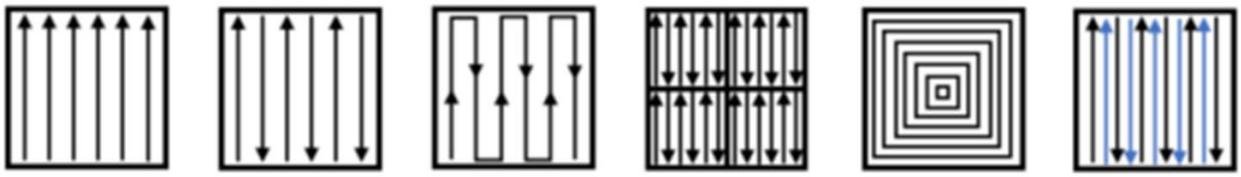

Figure 1: Most frequently used scan patterns in LPBF (Hamm, 2020).

A widespread scan pattern (Figure 1 b)) is the bidirectional scan, in which the laser alternately moves forwards and backwards and stops at the end of each path (Aboulkhair et al., 2014; Kempen et al., 2012; Thijs et al., 2013). Similar to this is the unidirectional scan (Figure 1 a)), in which the laser always scans in the same direction. The continuous scan (Figure 1 c)) also largely corresponds to the standard scan, except that the laser is no longer switched off, but scans continuously over the powder bed. This pattern is also called a zig-zag pattern or Z-shape (Han et al., 2020; Thijs et al., 2010). Figure 1 d) shows the island scan / chessboard scan, in which the length of the scan vectors is reduced by dividing the surface into smaller areas ("islands"). The scan pattern in Figure 1 e) is scanned in concentric circles or as multiple contour scans with the same contour path distance in each case. In re-melting (Figure 1 f)) each layer is scanned twice and thus each layer is melted twice.

Often, only individual scan strategies are compared with each other, whereby the scan strategy refers to the interaction of scan pattern, scan speed, scan sequence, rotation angle between the layers and other factors. With regard to the influence of the scan pattern on the mechanical properties of the component manufactured from AlSi10Mg using LPBF, a study by M. Guo et al. shows that the use of the chessboard pattern results in higher tensile strength, elongation at break,

density and hardness than a "linear" pattern. The term "linear scan pattern" refers to either a unidirectional or bidirectional pattern, which was not disclosed in the work of Guo (Guo et al., 2019). The difference between the scanning strategies is attributed to the higher number of pores of "linear" strategies. In addition, the chessboard strategy there shows a more uniform residual stress distribution in their samples.

In a comparison of concentric and bidirectional scan patterns for a similar aluminum alloy (Al-Si12), the concentric pattern was found to have a higher compressive load capacity (both for the scan sequence of concentric circles from inside to outside and from outside to inside, with the latter pattern having the highest overall load capacity) (Sairaiji et al., 2020). In another study by W. Ge et al. (Ge et al., 2014), a comparative analysis of the strategy without rotation and without re-melting (0°) versus the re-melting strategy with 90° rotation (*re90*) on a titanium alloy showed an approx. 33% increase in tensile strength for the former.

The use of different scan patterns also has an influence on the pore shape, number and distribution, which in turn can change the mechanical properties of the components. The use of the continuous compared to the bidirectional strategies leads to fewer pores at the inflection point of the laser paths and to a more uniform width of this path, which was observed by means of in-situ X-ray transmission by A.A. Martin et al. attributing it to the avoidance of the keyhole effect (Martin et al., 2019). A further comparison of the continuous, unidirectional and concentric scan pattern carried out by F. Léonard et al. shows a strong reduction in porosity for the concentric circles compared to the continuous scan paths and a high concentration of pores at the end of the scan paths for the unidirectional strategy. These observations were made by analyzing micro-computed tomography (µCT) scans, where two main positions of the pores could be found in the study: One agglomeration is caused by the "unloading" of pores at the end of the scan path (this is, for example, mainly responsible for the pores of the unidirectional strategy); the other agglomeration is related to the inflection point of the continuous strategy, causing a higher local porosity (Leonard et al., 2016). A global consideration of the porosity and density for the unidirectional and bidirectional scan pattern using optical microscopy shows a higher density for the bidirectional strategy in a comparison by J.P. Kruth et al. from 2010 (Kruth et al., 2010). Re-melting, in which each layer is scanned twice, has been investigated several times and in two different studies leads to a sharp decrease in porosity in the components, especially for a lower laser power during the second scan (experiments with Ti6Al4V and stainless steel) (Kruth et al., 2010; Yasa et al., 2011). This effect could also be demonstrated for AlSi10Mg and was greatest in a study by N.T. Aboulkhair for a reduction in laser power in the first scan (Aboulkhair et al., 2014; Liu et al., 2019).

Remelting also reduces the surface roughness of the components produced in this way (Kruth et al., 2010; Liu et al., 2019; Yasa et al., 2011). The order of the scan modes also has an influence on this; the surface roughness is lower if the contour scan is performed first and then the filling scan (Poncelet et al., 2018). When comparing bidirectional, continuous and concentric scan patterns, it becomes clear that the concentric strategy has the lowest roughness of these three scan patterns (Yeung et al., 2017).

As each layer is produced individually during selective laser melting, it is possible to change the angle of the scan direction for each layer. This change is referred to as the rotation angle θ. The rotation angle can be changed as desired, but the angle θ=67° is considered optimal according to a patent by M. Dimter et al. from 2008, as it should reduce deformations, anisotropy, the number of

defects and therefore improve the mechanical properties. The value of 67° was chosen because with this rotation for the maximum number of layers the direction of the scan vector is not repeated. M. Dimter et al. describe that for the angle θ=67° this is only possible after 360 layers and only after 18 layers does an orientation occur that is within 10° of an angle already used (Dimter et al., 2011). Similarly, θ=90° is also frequently used and, according to J.H. Robinson et al. (2019), is the "most common" angle, although 67° is described as "more suitable" (Robinson et al., 2019). 90° rotation between the layers changes the micro- and macrostructure in such a way that a more isotropic structure can be found in such a component compared to a component manufactured without rotation (Thijs et al., 2013). An influence of 90° rotation on the defects (reduction of pores) and on the strength and yield strength was also found (increase in both values) (Dai et al., 2018). For other materials, the change in the angle of rotation has different effects: For a titanium alloy, 18 different scanning strategies focusing on the rotation angle were investigated. However, the differences in density, surface roughness and strength between the investigated samples were not significant and therefore the rotation angle was not considered an influencing factor for the mechanical properties of the component (Robinson et al., 2019). For stainless steel, a higher yield strength, tensile strength and elongation at break were found for the rotation angle θ = 105°(Guan et al., 2013). For the iron-nickel alloy Invar, a lower number of pores was found for the rotation angle θ = 107° than for θ = 67° (Ertay et al., 2018). There is no uniform, scientifically based standard for the rotation angle, as the results for its variation are not always consistent and there is hardly any data available for the alloy AlSi10Mg. By directly comparing different rotation angles, its influence on the mechanical properties will be investigated experimentally in the following.

A comparative analysis of all the scan patterns presented and other scan patterns in combination with orientation angle and remelting with regard to their porosity distribution and correlation to mechanical strength has not yet been carried out and is subject of this work. Additional investigations into the resulting porosity and typical pore morphologies of different scan patterns are necessary in order to be able to draw conclusions about the safety and properties of the components produced in this way. A low surface roughness is important for a less complex post-processing of the components, so that further investigations should also confirm the influence of the scan pattern.

Methods

The specimens were fabricated using gas atomized AlSi10Mg powder supplied by m4p GmbH on an ORLAS CREATOR LPBF printer from O.R. Lasertechnologie GmbH. The chemical composition of the powder is shown in Table 1 (right). The powder had a D10 of 21.0 µm, D50 of 35.3 µm and a D90 of 57.5 µm with a bulk density of 1.5 g/cm^3. The CREATOR works with a Yb fiber laser with a power of up to 250 W and a wavelength of 1070 nm as well as an F-theta precision lens. An aluminum plate with a thickness of 14 mm and a diameter of 110 mm is used as the build platform. The powder reservoir is 120 mm wide in diameter and 210 mm deep. The CREATOR distributes the metal powder using a rotary coater with a speed of up to 35°/s. Processing takes place in an Argon inert gas atmosphere. The parameters for the production of the samples were kept constant with the exception of the scan parameters determining the pattern of scan vector placement. Optimized parameters were used, which were determined in previous tests. The constant values of the most important parameters can be found in Table 1 (left).

Table 1: Common parameters for preparing the samples (left) and chemical composition of the AlSi10Mg alloy (right).

Parameter	Value
Laser power	230 W
Beam diameter	40 µm
Scanning speed	950 mm/s
Path distance	125 µm
Contour path distance	125 µm
Layer thickness	30 µm

Element	Fe	Si	Mg	Mn	Ti	Zn
Mass fraction (%)	0,14	9,8	0,31	<0,01	0,01	0,01
	Cu	**Pb**	**Sn**	**Ni**	**Al**	
	<0,01	<0,01	<0,01	<0,01	base	

All samples were manufactured vertically. Cylindrical specimen geometries were used (see Figure 2) in their as-built condition with no further surface or heat treatment. As the anisotropy of components manufactured using LPBF has already been demonstrated in various studies, this effect was not investigated in this work. The specimens were fabricated using 15 different scanning strategies, which are shown in Figure *3*. It should be noted that *bi*, *cf*, and *67°* are equivalent strategies and are only presented separately for a better comparison of the changes made to the different aspects (i.e. rotation angle, direction, perimeter etc.) of the scanning strategies. In the later sections of this work, "*bi*" will be used to denote the results of this strategy.

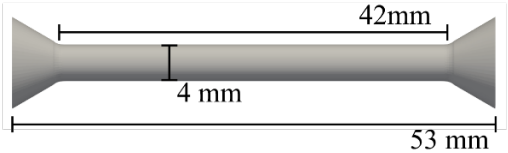

Figure 2: Cylindrical specimen geometry.

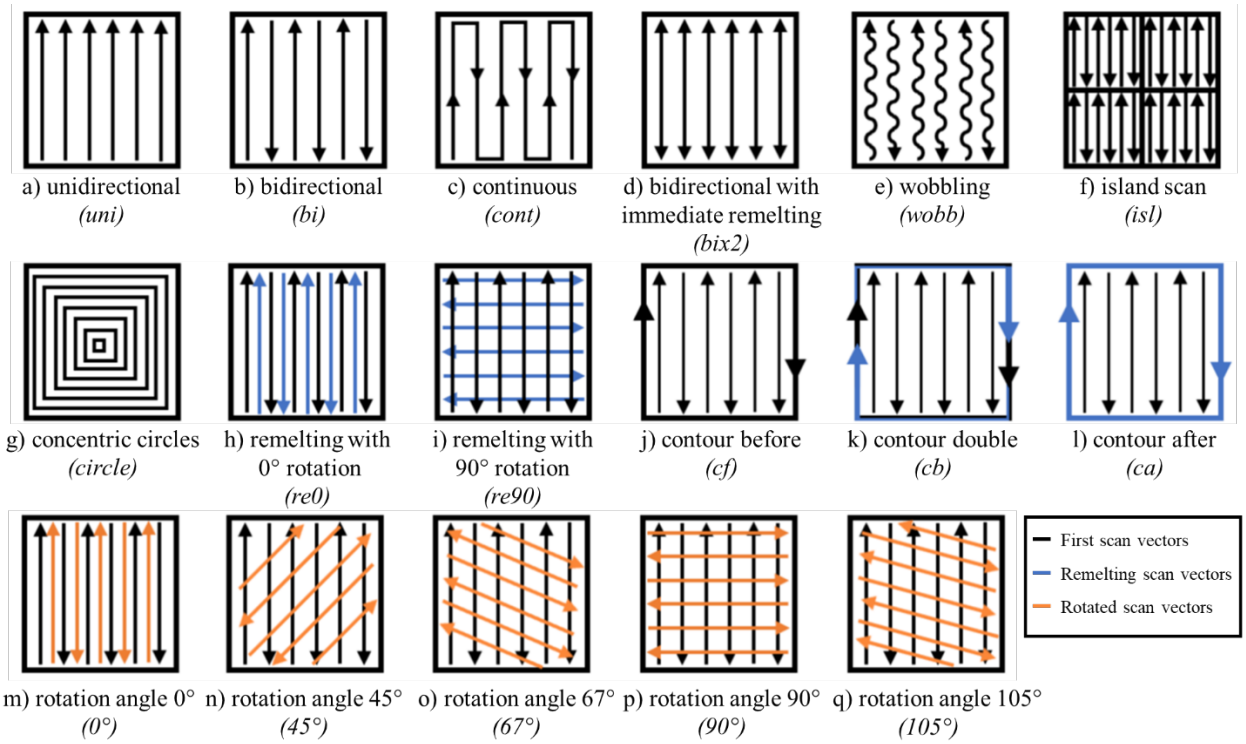

Figure 3: Overview of the scanning strategies used for the manufacturing of tensile samples and respective abbreviations in this study after (Hamm, 2020).

Five samples were produced from each scanning strategy in order to recognize any outliers and to be able to compare the mean values of the results. A total of 75 tensile samples were therefore produced, which were distributed across three prints. Care was taken to ensure that each scanning strategy was present in each of the three manufacturing processes and that their positions on the build platform were varied in the three prints in order to prevent factors such as manufacturing sequence, position on the build platform from influencing the results. Each print took about 8:30 hours.

The density of the tensile samples was determined using Archimedes' principle. The sample was weighed in air and in water and the density of the weighed body was calculated with the aid of the known data density of air and density of water (temperature-dependent). An ME-T analytical balance, which can be read to an accuracy of 0.1 mg, and a density kit from Mettler Toledo were used. To get a more detailed picture of the porosity, several µCT scans were also performed. The µCT scan was performed with a YXLON µCT Precision from YXLON International with a Perkin Elmer 1621 AN detector with 2048x2048 pixel. The acceleration voltage used for the X-ray microfocus tube FXE 225.99 was 165 kV and the current was 0.02 mA. The data generated consisted of 1860 projections. The resulting voxel edge length was 3 µm. The µCT was performed for a total of 10 samples. The acquired data was analyzed using the VGStudio Max software from Volume Graphics and Fiji/ImageJ. The images from the µCT scans were converted into Z-projections with ImageJ, i.e. into a 2D representation in which the pores from all Z-slices are projected onto a plane. With 1472 Z-slices each, this means that the Z-projections represent the pores from volume of approximately 4.74 mm in height. By setting a constant threshold value, these Z-projections were then converted into a black and white representation. In VGStudio Max, after a surface determination, a porosity analysis was performed with the "EasyPore" algorithm,

which automatically optimized the local threshold for porosity detection. The total number of pores as well as the diameter, volume and sphericity of each pore were recorded among other characteristics from the µCT images.

Using a µsurf confocal microscope from NanoFocus (Oberhausen, Germany), the surface topography of 15 samples (one sample for each scanning strategy) could be recorded without contact. The surface was measured for one sample as an example in several areas of the surface parallel to the build direction. As the deviations were not significant, only one measurement was carried out on the parallel surface for all other samples on an evaluation area of 2.56 mm². For the samples, where differences in the surface perpendicular to the build direction were to be expected (*re90, re0, circle, bi, bix2, conti*), this surface was also analyzed. The data was analyzed using the µsoft software tool (also from NanoFocus) according to DIN EN ISO 25178-2:2020-02.

The strength, yield strength and elongation at break of all samples were determined using a tensile test. The system on which this was carried out was the ZMART.PRO 200 kN model from ZwickRoell (Ulm, Germany). An Xforce-P load cell with a maximum force of 20 kN and a multiXtens extensometer with accuracy class 0.5 in accordance with EN ISO 9513 were used. The tensile test was performed in accordance with DIN EN ISO 6892-1:2020-06 and method A2 "open loop", which is characterized by the use of a constant crosshead speed. The results were analyzed using the test software testXpert II (ZwickRoell, Ulm, Germany). In the tests, the diameter determined under the macroscope was used to determine the tensile strength for each tensile specimen. This method was chosen because the diameter determined with a micrometer sometimes showed significant deviations from the values determined using the macroscope. The reason for this is that the roughness of the surface is recognizable under the macroscope and can therefore be excluded from the measurement, whereas this is not possible with the micrometer.

Results and Discussion

The density of each sample was determined using Archimedes' principle and thus also the porosity resulting from the density. A µCT was then carried out for selected samples, whereby the porosity for a small section of the sample could be analyzed and data on the shape and number of pores could be obtained.

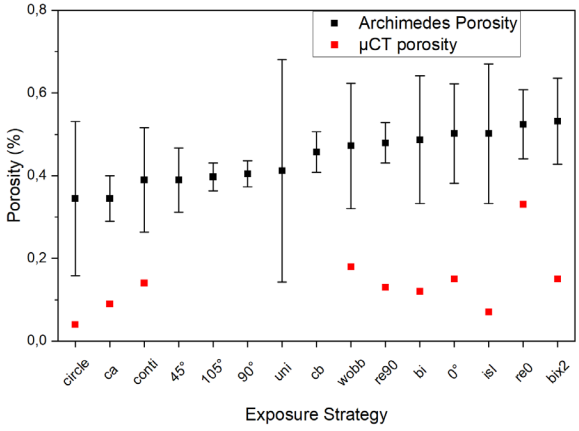

Figure 4: Porosity with standard deviation in dependence of scanning strategy in ascending order by Archimedes porosity.

For the strategies *bi, conti, bix2, isl, wobb, circle, ca, re0, re90* and *0°*, the porosity was also determined via µCT. This porosity was consistently lower than the porosity determined using the Archimedes method as shown in Figure 4. The density of the analyzed samples is over 99% for all samples. Compared to other studies in which the optimized parameters were investigated, the density values are in a similar order of magnitude or higher (see e.g. the range from 98.0% to 99.5% in (Kempen et al., 2011)). Furthermore, through using optimized parameters also densities above 99% could be achieved for remelting strategies (Aboulkhair et al., 2014). The results on the porosity of the analyzed samples show that the density or porosity measured using the Archimedes method does not correspond to the porosity from the µCT scan in all cases. This is due to the smaller statistics of µCT measured samples and the resolution limit of the µCT data through image noise and voxel size which obscures particularly small pores and therefore underestimates the overall porosity. Deviations in the density values identified using different methods are therefore possible. The data collected by the µCT scan can be used not only to make statements about the global porosity, but also to qualitatively describe the distribution of the pores and their shape. Figure 5 shows Z-projections (4.74 mm section height) of the images from the µCT scan for the individual strategies for easier comparison. It is striking that a ring of pores appears near the perimeter in all but the *circle*-type strategy. Several triangular porosity clusters are visible in the projection of the *isl*-strategy sample. The volume and sphericity analyzed for the 10 largest pores of each sample are further used for a correlation of the morphology with mechanical properties from the tensile tests.

Figure *6* g-i) shows that larger irregular pores occur for the strategies *re0, re90* and *ca*, which can be critical for failure. This is not recognizable from the global porosity or density, as this is 99.52% for *re90* (approximately the average of all samples - 99.56%) and 99.66% for *ca*, for example. The sparse occurrence of such irregular pores in strategies without re-melting indicates that the formation of irregular pores mainly occurs during the re-melting of already melted areas. The projection of the strategy *ca* (contour after filling scan) confirms this assumption, as here the irregular pores mainly occur at the edge, where the area already produced by filling is melted again by applying the contour. This contrasts various early studies (Aboulkhair et al., 2014; Yasa et al., 2011) with the conclusion that re-melting reduces the existence of pores. A more recent study (Huang and Yeong, 2018) compared various studies on re-melting and its influence on density and concludes that a very high density similar to that achieved with low-power re-melting can also be achieved with a single scan at a higher laser power rather fitting the laser power used in this study. For all strategies except *circle*, a "ring" of pores can be recognized at the edge of the hatched area, where mainly irregular, but also spherical pores can be seen. This characteristic pattern is caused by briefly switching off the laser at the boundary of the fill scan area. During the scan, the laser pushes the spherical pores in the melt pool in front of it and they can settle at the end of the scan vector. The keyhole effect is also particularly prominent at the ends of the scan paths, as this is where the vapor capillary collapses and keyhole pores form. This observation is consistent with other studies that have found a similar pattern for the pores at the end of the scan vectors, such as (Thijs et al., 2013) for AlSi10Mg or (Leonard et al., 2016).

Equally consistent with this behavior is the observation that for the *0°* strategy these pores were mainly found at two opposite ends and often at the same points, since without rotation between the layers the start and end of the scan paths always fall on the same points. The *circle* strategy, on the other hand, did not show a ring, as there are no start and end points at the edge of the sample due to the concentric paths, but a dominant pore area is also visible at the start or end of the individual

concentric circular paths with this strategy. With the *isl* strategy, several of these pore rings could be observed, which is due to the division of the area to be scanned into smaller areas. This also reduces the concentration of pores at the outer edge with *isl.*

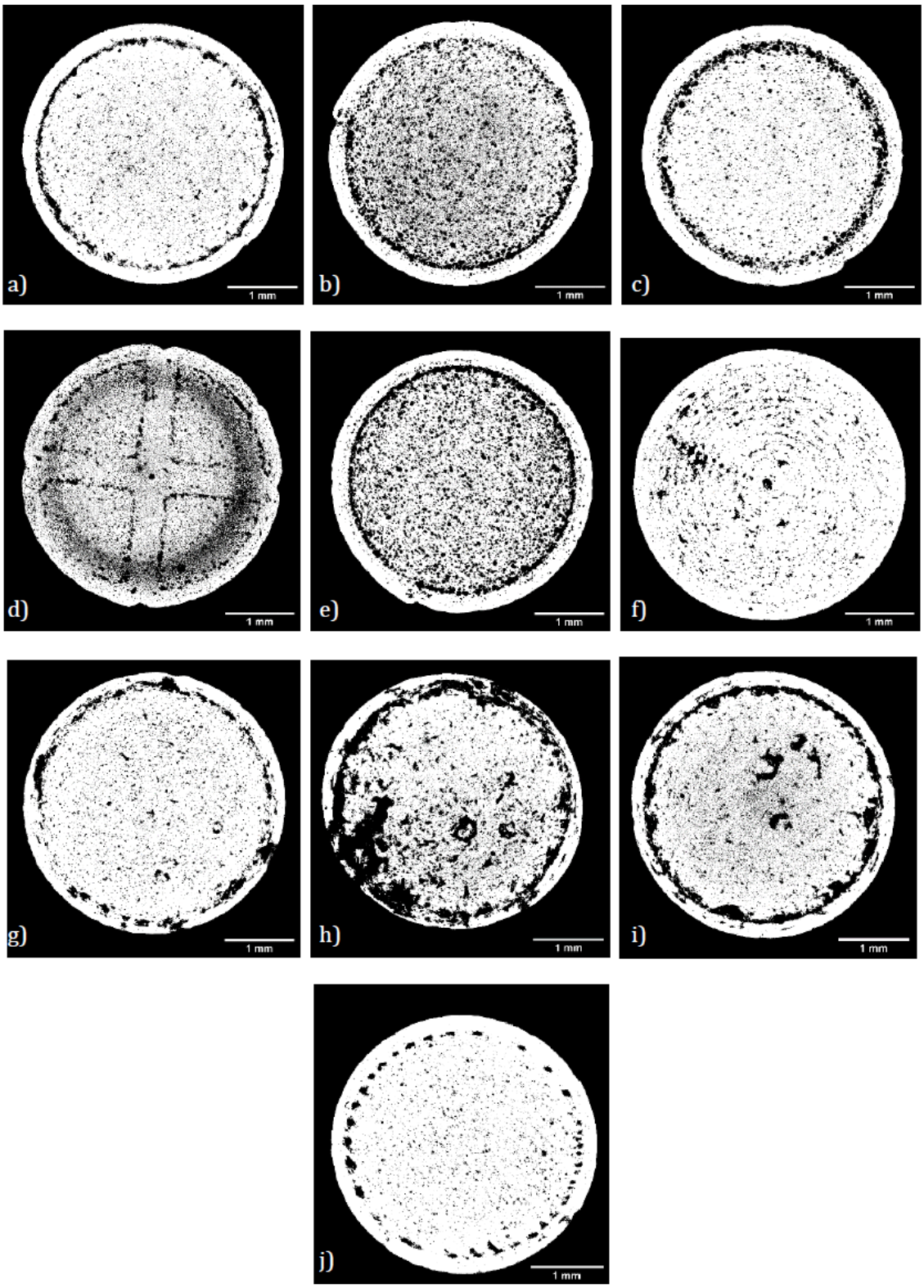

Figure 5: Projections of the µCT images in the Z direction of the scanned sample sections (pores shown in dark): a) *bi*, b) *conti*, c) *bix2*, d) *isl*, e) *wobb*, f) *circle*, g) *ca*, h) *re0*, i) *re90*, j) *0°* in (Hamm, 2020).

It is noticeable that with the *conti* and *wobb* strategies, many and almost exclusively very spherical pores can be recognized, which are distributed over the entire filling scan surface. The reason for the *conti* strategy could be that the laser is not switched off at the end of the scan path and thus the metallurgical pores cannot settle, which leads to them being distributed in the melt pool. No reason could be found for the *wobb* strategy, but according to a patent by (Pavlov et al., 2019), this leads to lower temperature gradients and wider melt pools, which may favor the distribution of metallurgical pores within the melt pool.

By comparing the data of the 10 largest pores, the statements made from the visual analysis of the projections can be confirmed (see Figure 6): For the strategies *re0, re90* and *ca*, the average volume of the 10 largest pores is significantly higher than for the other strategies and for the strategies *conti* and *wobb*, a higher sphericity of the 10 largest pores can be recognized than for the other strategies analyzed. The absolute number of pores is also highest for the *conti* and *wobb* strategies. It can be concluded that the number, localization and shape of the pores are not left to chance, but occur differently depending on the scanning strategy used due to various mechanisms. In particular, it can be seen that re-melting at a laser power that already leads to a sufficiently high density in a single scan tends to have negative effects on pore formation, both in terms of pore size and shape. This can be explained similar to pore formation at very small hatching distances, where due to the change in reflectivity for the metal surface and the increase in heat conduction the melt pool geometry changes and creates balling effect within former stable process windows. However, this cannot be recognized without a µCT image of the sample and its analysis, as the global porosity can be approximately average due to the higher number of spherical pores in other strategies. Another effect that can be observed in almost all strategies is the pore ring at the edge of the filling scan area, which is due to the laser power density change at the end of the scan paths and which favors the occurrence of both metallurgical (spherical) and irregular pores (keyhole pores). This effect occurs least for the *conti* and the *circle* strategy, which leads to the assumption that these strategies are the best for PBF-LB manufacturing with a non-critical pore morphology.

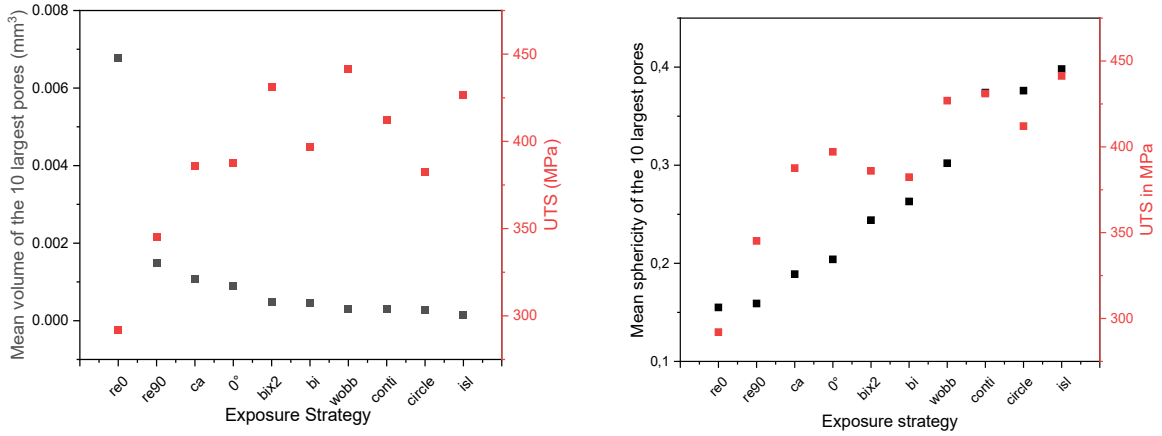

Figure 6: Correlation of mean volume (left) of the 10 largest pores (descending) and mean sphericity (right) of the 10 largest pores (ascending) respectively with tensile strength UTS. UTS is taken only from the specimen, which was µCT scanned and is not an average value.

In Figure 7, the surface roughness Sa and Sz for the different strategies is depicted. A distinction is made between the roughness of the surface parallel to the build direction (Z direction) and the surface perpendicular to the build direction. A low roughness of the surface perpendicular to the build direction ("top") does not correlate with a low roughness of the surface parallel to the build direction, but the maximum roughness Sa for both surfaces is around 20 µm and the minimum roughness is not less than 5 µm.

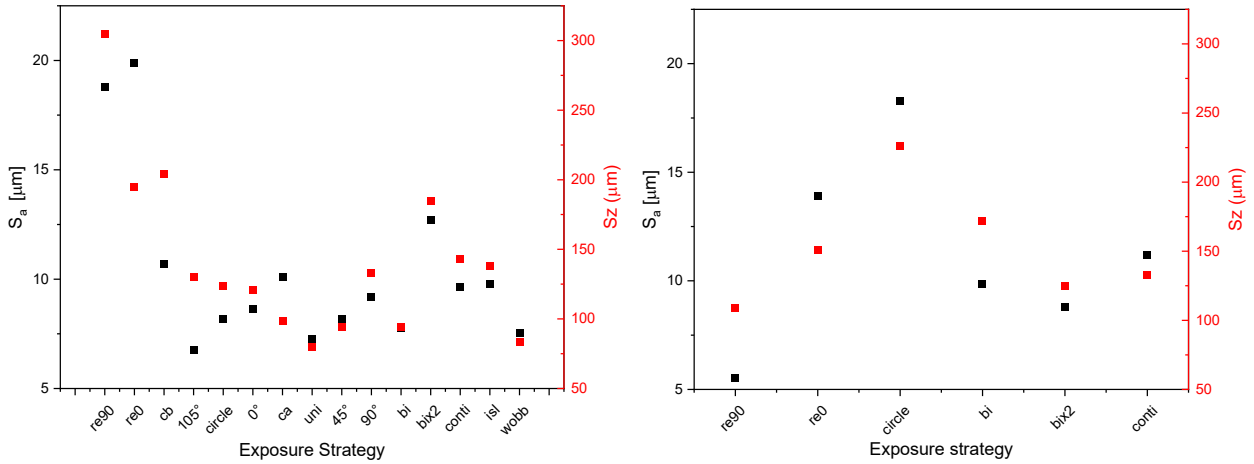

Figure 7: Surface roughness Sa and Sz in µm for different scanning strategies on the surfaces parallel to the build direction (left) and perpendicular to the build direction (right).

Spatter due to increased energy input is the probable cause for the particularly rough surfaces (see Figure 8). For the surfaces parallel to the build direction, *re0, re90* and *bix2* were clearly the strategies with the highest roughness value while for the surfaces perpendicular to the build direction the *circle*- and *re0*-strategy exhibit the highest roughness values. The remaining strategies all had a similar average surface roughness between Sa ≈ 5 µm and Sa ≈ 11 µm.

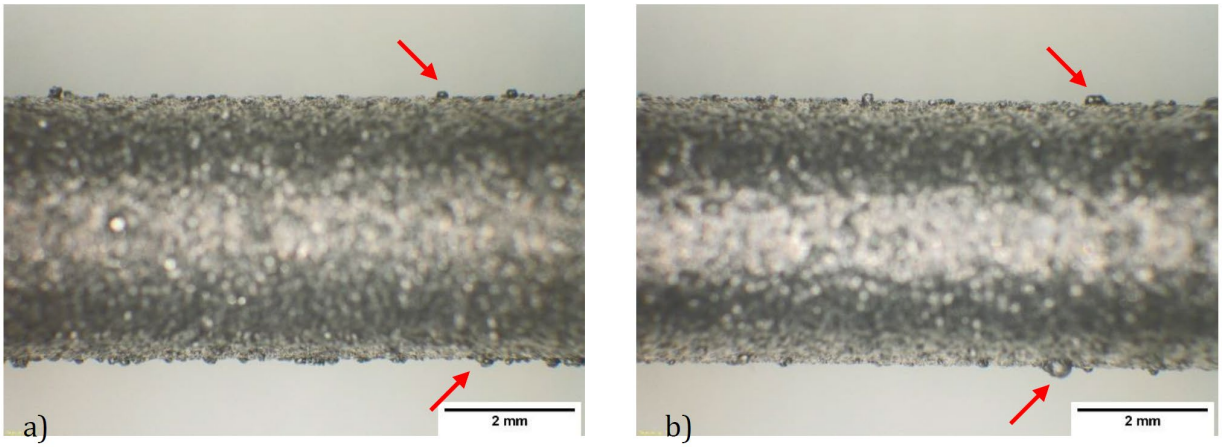

Figure 8: Images from the macroscope, round adhesions on the surface a) strategy *re0*, b) strategy *re90.*

In the literature, E. Yasa et al. and S. Huang et al. pointed out that so-called "laser surface remelting", LSR for short, can improve the surface quality and reduce the surface roughness. In these, re-melting is only applied to the top, i.e. the last, layer of in the build process, which is described as time-saving compared to general re-melting (Huang and Yeong, 2018; Yasa et al.,

2011). However, contrary to this work, the studies were not carried out with AlSi10Mg and the re-melting was carried out after removing the powder. Another study (Liu et al., 2019) compares the *bi* and *re0* strategies for AlSi10Mg and concludes that the *re0* strategy results in a lower surface roughness than *bi*. For the measurement carried out in this work, a similar significant reduction in surface roughness can be seen for the *re90* strategy (from *bi* Sa = 9.86 µm to *re90* Sa = 5.52 µm). The change in roughness for different contour sequences can be deduced from Figure 7 as it clearly shows that the *bi* strategy (which is also *cf*) has the lowest surface roughness with Sa = 7.79 µm and *ca* (Sa = 10.1 µm) and *cb* (Sa = 10.7 µm) have a similar, but higher, roughness. This was also confirmed by (Poncelet et al., 2018) who compared the *cf* and *ca* strategies in their work and consistently found a lower surface roughness for *cf* for different offset parameters and laser powers. Overall, it can be assessed, that re-melting leads to a higher roughness on the surface parallel to the build direction, which can be attributed to the increase in energy density on an already warm substrate as well as the drawing in of additional metal powder to the surface from the powder bed. For the surface perpendicular to the build direction, the effect described in other studies of improving the surface roughness when re-melting could only be demonstrated to a limited extent for the *re90*-strategy.

The overall strength values measured in this work are comparable with those in the literature (Buchbinder et al., 2015; Hitzler et al., 2017; Kempen et al., 2012; Yan et al., 2020), although not all 15 scanning strategies investigated in this work have been compared or evaluated in the literature. Basically, it can be said that the results obtained for the tensile strength UTS, the 0.2 % proof stress Rp0.2 and the elongation at break A_{20} were within the expected range (see Figure *9*). A similar picture emerged for the tensile strength and elongation at break, with the *conti, isl* and *wobb* scanning strategies having the highest values and also exhibiting average to very low variation in the individual samples. These strategies can therefore be rated as particularly reliable. However, the re-melting strategies, in particular *re0* and *re90*, exhibited high fluctuations and low tensile strengths, which means that the part behavior cannot be predicted reliably and the strategies should be assessed as rather unfavorable. Like the density, the mechanical properties from the tensile test showed high and expected values, with the average UTS = 399.2 MPa, the 0.2 % proof stress at Rp0.2 = 230.9 MPa and the elongation at break at A_{20} = 3.1 %. The order of the strategies was similar for UTS and A_{20}, with *conti, isl* and *wobb* each having the highest values. All strategies had a similar value for the yield strength, which varied little between samples of the same strategy. Pore morphology was therefore identified as the reason for the different tensile strength values and elongation at break, as both the average size of the 10 largest pores and the sphericity of these showed a strong correlation with the tensile strength (see Figure 6). The global density (average porosity was 0.44%), on the other hand, did not appear to be relevant for the tensile strength.

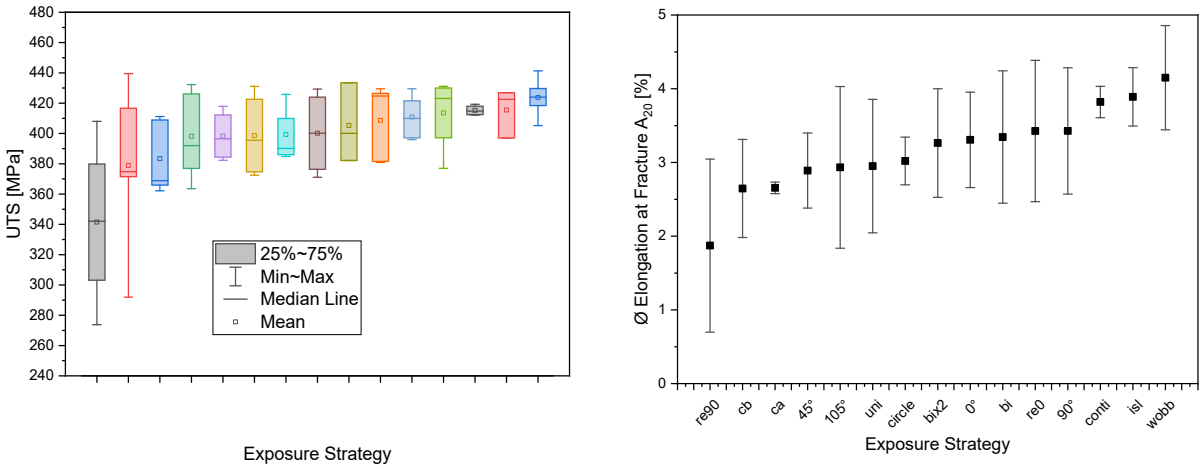

Figure 9: UTS of the investigated exposure strategies with statistic evaluation (left) and elongation at fracture A_{20} with standard deviation in ascending order (right).

Via XCT measurements metallurgical as well as keyhole and lack-of-fusion pores were found. A high number of spherical pores was observed for the *conti* and *wobb* strategies and particularly large and many irregular pores for the *re90* and *re0* strategies. An increased concentration of pores at the end points of the laser paths was confirmed for all strategies, which is consistent with the findings in literature. From the porosity characteristics the strong interaction of the tensile strength UTS and the average volume of the 10 largest pores is shown by the rank correlation coefficient of $r_\tau = -0.51$ according to Kendall which is significant at the level p=0.05. Therefore, the UTS increases for a lower average pore volume. The connection between the sphericity of the pores in the individual samples and the UTS was also investigated, as can be seen in Figure 6 (right). Here the rank correlation coefficient is significant at the p=0.05 level with $r_\tau = 0.69$ indicating a very strong correlation. As the positive coefficient proves, the lowest UTS was measured for the samples with the lowest sphericity and the highest tensile strength was measured for the samples with the highest sphericity.

With regard to the assessment of the individual strategies, it can be concluded that the re-melting strategies *re0* and *re90* have a lower strength, a higher porosity in the µCT analysis, a higher average volume and a lower sphericity (i.e. an overall more critical pore morphology) as well as a higher surface roughness than the strategies in which the sample is only scanned once. Re-melting is therefore not recommended for LPBF with sufficiently high laser power and, as a result, a sufficiently high density. The strategies, some of which do not have a particularly high density but a non-critical pore morphology (smaller and rounder), i.e. *conti, wobb* and *isl* in particular, are those for which a high tensile strength was measured and a high elongation at break; therefore the more recommendable ones. Although *67°* was identified as the "best" strategy for the strategies with different rotation angles, the differences in these strategies (*0°, 45°, 67°, 90°* and *105°*) are so small that they cannot be classified as significant. The order of the contour scan had little influence on the strength, but based on the low surface roughness, the standard strategy *cf* is the one that should most likely be used, as the remelting of the contour scan does not improve any of the properties investigated. The remaining strategies, i.e. *bi, bix2, circle* and *uni*, showed expectedly high tensile strength and yield strength values, average surface roughness and a similar micro- and macrostructure.

Conclusions

This study investigated the impact of 15 different scanning strategies on AlSi10Mg specimens fabricated via selective laser melting. Strategies included varying scan patterns, contour sequences, re-melting approaches and layer rotation angles. Significant differences in mechanical properties were noted among strategies, particularly affecting tensile strength and elongation at break. Porosity levels averaged at 0.44%, with distinct pore morphologies observed across different strategies impacting mechanical performance. Surface roughness analysis highlighted variations attributable to energy input, with certain strategies exhibiting notably rougher surfaces. Tensile testing revealed average strengths of UTS = 399.2 MPa with strategy-specific variations observed. Strategies involving re-melting generally showed lower strength and higher roughness compared to single-scan strategies. Overall, the study underscores the critical influence of scanning strategy on process porosity distributions and correlated mechanical properties in LPBF, offering insights for optimizing manufacturing parameters and enhancing performance outcomes.

References

Aboulkhair, N.T., Everitt, N.M., Ashcroft, I., Tuck, C., 2014. Reducing porosity in AlSi10Mg parts processed by selective laser melting. Additive Manufacturing 1–4, 77–86. https://doi.org/10.1016/j.addma.2014.08.001

Aboulkhair, N.T., Maskery, I., Tuck, C., Ashcroft, I., Everitt, N.M., 2016. On the formation of AlSi10Mg single tracks and layers in selective laser melting: Microstructure and nano-mechanical properties. Journal of Materials Processing Technology 230, 88–98. https://doi.org/10.1016/j.jmatprotec.2015.11.016

Buchbinder, D., Meiners, W., Wissenbach, K., Poprawe, R., 2015. Selective laser melting of aluminum die-cast alloy—Correlations between process parameters, solidification conditions, and resulting mechanical properties. Journal of Laser Applications 27, S29205. https://doi.org/10.2351/1.4906389

Dai, D., Gu, D., Zhang, H., Xiong, J., Ma, C., Hong, C., Poprawe, R., 2018. Influence of scan strategy and molten pool configuration on microstructures and tensile properties of selective laser melting additive manufactured aluminum based parts. Optics & Laser Technology 99, 91–100. https://doi.org/10.1016/j.optlastec.2017.08.015

Dimter, M., Mayer, R., Hümmeler, L., Salzberger, R., Kotila, J., Syvänen, T., 2011. Method and device for manufacturing a three-dimensional object.

Ertay, D.S., Ma, H., Vlasea, M., 2018. Correlative beam path and pore defect space analysis for modulated powder bed laser fusion process.

Ge, W., Lin, F., Guo, C., 2014. The effect of scan pattern on microstructure evolution and mechanical properties in electron beam melting Ti47Al2Cr2Nb.

Guan, K., Wang, Z., Gao, M., Li, X., Zeng, X., 2013. Effects of processing parameters on tensile properties of selective laser melted 304 stainless steel. Materials & Design 50, 581–586. https://doi.org/10.1016/j.matdes.2013.03.056

Guo, M., Ye, Y., Jiang, X., Wang, L., 2019. Microstructure, Mechanical Properties and Residual Stress of Selective Laser Melted AlSi10Mg. J. of Materi Eng and Perform 28, 6753–6760. https://doi.org/10.1007/s11665-019-04423-2

Hamm, A.V., 2020. Influence of laser scan strategy on mechanical properties of SLM fabricated parts (Bachelor Thesis). Karlsruhe Institute of Technology, Karlsruhe.

Han, J., Wu, M., Duan, W., 2020. A Proposed Scan Strategy Used on SLM Inner Structure Part. Materials 13, 937. https://doi.org/10.3390/ma13040937
Hitzler, L., Janousch, C., Schanz, J., Merkel, M., Heine, B., Mack, F., Hall, W., Öchsner, A., 2017. Direction and location dependency of selective laser melted AlSi10Mg specimens. Journal of Materials Processing Technology 243, 48–61. https://doi.org/10.1016/j.jmatprotec.2016.11.029
Huang, S., Yeong, W.Y., 2018. Laser re-scanning strategy in selective laser melting for part quality enhancement: A review.
Kempen, K., Thijs, L., Van Humbeeck, J., Kruth, J.-P., 2012. Mechanical Properties of AlSi10Mg Produced by Selective Laser Melting. Physics Procedia 39, 439–446. https://doi.org/10.1016/j.phpro.2012.10.059
Kempen, K., Thijs, L., Yasa, E., Badrossamay, M., Verheecke, W., Kruth, J.-P., 2011. Process optimization and microstructural analysis for selective laser melting of AlSi10Mg.
Kruth, J.-P., Badrossamay, M., Yasa, E., Deckers, J., Thijs, L., Van Humbeeck, J., 2010. Part and material properties in selective laser melting of metals, in: Proceedings of the 16th International Symposium on Electromachining (ISEM XVI). Shanghai Jiao Tong Univ Press, pp. 3–14.
Leonard, F., Tammas-Williams, S., Todd, I., 2016. CT for Additive Manufacturing Process Characterisation: Assessment of melt strategies on defect population.
Liu, B., Li, B.-Q., Li, Z., 2019. Selective laser remelting of an additive layer manufacturing process on AlSi10Mg. Results in Physics 12, 982–988. https://doi.org/10.1016/j.rinp.2018.12.018
Martin, A.A., Calta, N.P., Khairallah, S.A., Wang, J., Depond, P.J., Fong, A.Y., Thampy, V., Guss, G.M., Kiss, A.M., Stone, K.H., Tassone, C.J., Nelson Weker, J., Toney, M.F., Van Buuren, T., Matthews, M.J., 2019. Dynamics of pore formation during laser powder bed fusion additive manufacturing. Nat Commun 10, 1987. https://doi.org/10.1038/s41467-019-10009-2
Pavlov, M., Hoebel, M., Roerig, F., Schurb, J., 2019. Method for manufacturing a metallic or ceramic component by selective laser melting additive manufacturing. US10337335B2.
Poncelet, O., Van Der Rest, C., Marteleur, M., Simar, A., 2018. Effect of scan strategy and laser parameters on roughness of SLM AlSi10Mg thin-walls, in: 3rd Workshop on Metal Additive Manufacturing.
Robinson, J.H., Ashton, I.R.T., Jones, E., Fox, P., Sutcliffe, C., 2019. The effect of hatch angle rotation on parts manufactured using selective laser melting. RPJ 25, 289–298. https://doi.org/10.1108/RPJ-06-2017-0111
Sairaiji, M., Yoshizaki, H., Iwaoka, H., Hirosawa, S., Maruo, S., 2020. Effect of Scan Strategy on Mechanical Properties of AlSi12 Lattice Fabricated by Selective Laser Melting. Journal of Laser Micro Nanoengineering 15, 1–5.
Thijs, L., Kempen, K., Kruth, J.-P., Van Humbeeck, J., 2013. Fine-structured aluminium products with controllable texture by selective laser melting of pre-alloyed AlSi10Mg powder. Acta Materialia 61, 1809–1819. https://doi.org/10.1016/j.actamat.2012.11.052
Thijs, L., Verhaeghe, F., Craeghs, T., Humbeeck, J.V., Kruth, J.-P., 2010. A study of the microstructural evolution during selective laser melting of Ti–6Al–4V. Acta Materialia 58, 3303–3312. https://doi.org/10.1016/j.actamat.2010.02.004
Tradowsky, U., White, J., Ward, R.M., Read, N., Reimers, W., Attallah, M.M., 2016. Selective laser melting of AlSi10Mg: Influence of post-processing on the microstructural and

tensile properties development. Materials & Design 105, 212–222. https://doi.org/10.1016/j.matdes.2016.05.066
Yan, Q., Song, B., Shi, Y., 2020. Comparative study of performance comparison of AlSi10Mg alloy prepared by selective laser melting and casting. Journal of Materials Science & Technology 41, 199–208. https://doi.org/10.1016/j.jmst.2019.08.049
Yasa, E., Deckers, J., Kruth, J., 2011. The investigation of the influence of laser re-melting on density, surface quality and microstructure of selective laser melting parts. Rapid Prototyping Journal 17, 312–327. https://doi.org/10.1108/13552541111156450
Yeung, H., Lane, B., Fox, J., Kim, F., Heigel, J., Neira, J., 2017. Continuous laser scan strategy for faster build speeds in laser powder bed fusion system.